Growing N-doped multiphase TiO_2 nanocomposites on reduced graphene oxide

Ozer, Lütfiye Y.; Shin, Yuyoung; Felten, Alexandre; Oladipo, Habeebllah; Pikuda, Oluwadamilola; Muryn, Christopher; Casiraghi, Cinzia; Palmisano, Giovanni

Published in:
Journal of Environmental Chemical Engineering

DOI:
10.1016/j.jece.2017.09.042

Publication date:
2017

Document Version
Publisher's PDF, also known as Version of record

Journal of Environmental Chemical Engineering 5 (2017) 5091–5098

Contents lists available at ScienceDirect

Journal of Environmental Chemical Engineering

journal homepage: www.elsevier.com/locate/jece

Research Paper

Growing N-doped multiphase TiO_2 nanocomposites on reduced graphene oxide: Characterization and activity under low energy visible radiation

Lütfiye Y. Ozer[a], Yuyoung Shin[b], Alexandre Felten[c], Habeebllah Oladipo[a], Oluwadamilola Pikuda[a], Christopher Muryn[b], Cinzia Casiraghi[b], Giovanni Palmisano[a,*]

[a] Department of Chemical Engineering, Khalifa University of Science and Technology, Masdar Institute, Masdar City, PO Box 54224, Abu Dhabi, United Arab Emirates
[b] School of Chemistry, University of Manchester, Oxford road, Manchester, M139PL, United Kingdom
[c] Synthesis, Irradiation and Analysis of Materials (SIAM), University of Namur, rue de Bruxelles 61, Namur, 5000, Belgium

ARTICLE INFO

Keywords:
Photocatalysis
Reduced graphene oxide-TiO_2
Multiphase TiO_2
N-doping
Visible radiation

ABSTRACT

Reduced graphene oxide (G) was used as a platform to grow a mixed catalyst made of brookite and rutile nanoparticles doped with nitrogen, resulting in excellent performance for the oxidation of 4-nitrophenol (4-NP) in water under low energy (> 425 nm) radiation. The samples were fully characterized by X-Ray Diffractometry (XRD), Raman Spectroscopy, Electron Microscopy, X-Ray photoelectron spectroscopy (XPS), photoluminescence (PL), Z-potential analysis, UV–vis Diffuse Reflectance Spectrophotometry (UV–vis DRS), and porosimetry. The improved hole-electron separation, demonstrated by PL, is boosted by the exceptional properties of reduced graphene oxide, which attracts and conveys electrons to dissolved oxygen, in turn initiating the oxidation process. The optimal amount of reduced graphene oxide was found to be 1% w/w based on 4-nitrophenol (4-NP) conversion rates. No leaching of carbon into water was revealed, even under irradiation, pointing to the suitability of the composite catalyst in water.

1. Introduction

Photocatalysis is an increasingly popular technology to mitigate pollution and environmental issues [1–3]. As such, it enables the degradation of organic species in water without the use of aggressive oxidizing chemicals. TiO_2 has been the most widely reported photocatalyst owing to its low cost, high efficiency and good stability. However, the ability of TiO_2 to be activated for oxidation processes is restricted to the need of UV light. Consequently, its modification with nitrogen has been proved as one of the best way to boost reactivity under visible light radiation, which is the majority of solar spectrum, and the only light available indoors [4]. The most used crystal phase of TiO_2 is anatase (with a band gap of 3.2 eV), very active in the UV region; however, rutile and brookite-rutile nanocomposites have been recently reported to be active in the visible, especially upon nitrogen doping [5,6]. Rutile has a narrower band gap (3.0 eV) than anatase and, coupled with brookite, it can enhance charge separation. Nitrogen atoms can be incorporated either interstitially or substitutionally, acting as attraction centers for holes [7], and then foster the formation of oxygen vacancies, thus promoting absorption of visible light and, eventually, reactivity. Beside nitrogen doping, addition of reduced graphene oxide (G) can significantly enhance reactivity under visible radiation [8] due to its remarkable properties, such as high electron mobility, high surface area to volume ratio, because of its 2-dimensional nature, and transparency [8]. To the best of our knowledge, there was only one attempt to obtain a N-doped TiO_2 synthesized on graphene through a sol-gel route, giving rise to anatase phase; moreover, the catalyst was not used for water remediation purposes [9]. While the modification of anatase or anatase-rutile TiO_2 with reduced graphene oxide has been reported in the last years by a number of scholars [10,11], the present study deals with a new composite material (N-TiO_2-G) obtained by synthesizing N-doped brookite-rutile nanoparticles in the presence of reduced graphene oxide (G). The particles form and grow on the reduced graphene oxide sheets, resulting in a number of advantages in terms of 4-NP photodegradation in water, irradiated by visible LED, as detailed in the following. To the best of our knowledge, TiO_2 modified with reduced graphene oxide has never been used before to oxidize 4-NP.

2. Experimental

2.1. Synthesis of reduced graphene oxide

A modified Hummer method was used to prepare graphite oxide by

* Corresponding author.
E-mail address: gpalmisano@masdar.ac.ae (G. Palmisano).

http://dx.doi.org/10.1016/j.jece.2017.09.042
Received 13 June 2017; Received in revised form 17 September 2017; Accepted 21 September 2017
Available online 22 September 2017

using graphite flakes as the precursors. 3 g graphite flakes, 2.5 g potassium persulfate and 2.5 g phosphorous pentoxide were poured into 12 mL concentrated sulfuric acid (H_2SO_4) and stirred vigorously for 4.5 h at 80 °C. The mixture was cooled down to room temperature naturally. Afterwards, 0.5 L deionized (DI) water was added and aging was prolonged for 12 h under stirring. The solution was filtered, washed and dried to obtain a black solid. The pretreated graphite flakes underwent oxidation by 15 g potassium permanganate ($KMnO_4$) in 120 mL concentrated sulfuric acid (H_2SO_4) in an ice bath for 1 h. The mixture was stirred at 35 °C for 24 h to obtain a very viscous dark-brown paste, diluted with a slow addition of 250 mL of DI water and further stirred for 4 h 30 mL (30 w%) of H_2O_2 were slowly added to quench the solution thus producing a golden-brown solution. The mixture was filtered and washed with DI water until a pH of 6 was obtained in the washing solution. The graphite oxide was dried at 40 °C. Following the oxidation process, graphite oxide (0.5 g L^{-1}) was exfoliated in water using an ultrasound bath (100 W) for 10 h, ultimately producing a multilayered graphene oxide (GO). The reduction of GO was performed by using reducing agent, that is sodium borohydride ($NaBH_4$), by stirring at room temperature for 5 h. Reduced graphene oxide (G) black powder was finally dried by a rotary evaporator at 50 °C. Washing with DI water 10 times with the aid of a centrifuge removed the residual ions producing a pure G powder.

2.2. Fabrication of N-TiO_2-G

N-TiO_2-G was prepared by using a sol-gel method. Titanium (IV) butoxide (TBOT) was used as TiO_2 precursor. TBOT, 2-propanol and HCl (4 M) in a volumetric ratio of 1:5.461:1.283, respectively, were mixed until a clear solution (total volume: 116.24 mL) was obtained under stirring at 70 °C for 20 h. The samples were dried by means of rotary evaporator at 70 °C. Following that, the powder was calcined at 450 °C for 4 h under nitrogen flow to minimize oxidative/thermal degradation of G. G and ammonium nitrate, used as N-doping agent with 0.8% (w/w), were dispersed/dissolved in the water prior to mixing with TBOT, HCl and 2-propanol solution. When needed, ultrasound treatment and ultrafast (3000 rpm) magnetic stirring were applied to properly break down and disperse G. Bare N-doped TiO_2 was prepared as well. The amount of G was fixed at 0.1%,0.5% 1%, 1.5%, 2% (w/w) with respect to TiO_2 and the corresponding samples were denoted as N-TiO_2/G_0.1%, N-TiO_2-G_0.5%, N-TiO_2-G_1%, N-TiO_2-G_1.5% and TiO_2-G_2%, respectively.

2.3. Characterization and reactivity – experimental details

A Nova NanoSEM was used to observe the morphology and dimensions of samples and to perform EDX mapping. Samples were prepared by dropping a water suspension on a stainless steel stub previously cleansed with water, acetone and ethanol under ultrasounds. Mapping of the constitutive elements of the composite materials was carried out by using a distribution mapping technique by energy dispersive X-ray spectroscopy (EDX) combined with SEM. EDX mapping was recorded using a spot size of 5 nm, X-ray energy of 20 eV with a 256 × 200 resolution and 200 μs dwells (64 frames). Carbon, titanium and oxygen mapping, using red, green and blue colors respectively, provides the visualization of elemental contents.

Powder X-Ray diffraction (XRD) was performed in a 2θ range of 10–90° by using PANalytical Empyrean diffractometer with Cu Kα radiation of 1.54 Å at 45 kV and 40 mA to determine the crystal structure of the prepared samples. The powders were ground in a mortar before analysis, and a holder with fixed thickness of samples was used to get comparable results.

Raman spectroscopy was performed by a Renishaw Raman spectroscope equipped with a 514.5 nm laser line and laser power below 0.5 mW. The Raman spectra were collected in back scattering configuration in the range 3500 cm^{-1}–50 cm^{-1}. The powder was pressed in a holder to get a homogeneous surface before the analysis.

Fourier transform infrared (FT-IR) analysis was carried out by using a Bruker Vertex 80 v FT-IR (128 scans) in the 4000 cm^{-1}–400 cm^{-1} region in diffuse reflectance mode (DRIFT). The powders were ground in a mortar before analysis and pressed in a holder to get a flat surface.

X-ray Photoelectron Spectroscopy (XPS) was performed on an Escalab 250 × i from Thermo with a monochromatic Al Kα source (1486.6 eV). Photoelectrons are collected at an angle of 0° relative to the sample surface normal. Samples were fixed using double-sided carbon tape. Survey and high-resolution spectra were acquired using a spot size of 250 μm and pass energy of 150 eV and 20 eV, respectively. A flood gun with combined electron and low energy ions was also used during analysis to prevent surface charging. Surveys were measured in steps of 1.0 eV with 50 ms dwell time per data point. Nitrogen, carbon, and oxygen 1 s high-resolution spectra were measured within the spectral range of interest with 0.1 eV steps and 50 ms dwell time per data point. Analysis of the data was carried out with CasaXPS software. A Shirley background was used in curve-fitting along with a GL(30) line-shape (70% Gaussian, 30% Lorentzian using the Gaussian/Lorentzian product form) for the C 1s, N 1s and O 1s spectra. Samples were referenced to the C 1s emission by adventitious hydrocarbon contamination at 284.8 eV.

TEM analysis was carried out by using a Tecnai G2 transmission electron microscope to observe the morphology and dimensions of samples. Samples for TEM were deposited on a Forvar/Carbon 300 or 400-mesh Cu grid purchased from Tedpella; the powder was previously suspended in water and 2 μL were dropped on the TEM grid twice (waiting for the complete drying before the second deposition).

The adsorption/desorption isotherms of the catalysts were recorded by using a Quantachrome NOVA 2000e surface area and pore size analyzer by using N_2 as adsorbent. The sample was degassed in static conditions under vacuum at 400 °C for 4 h prior to analysis. The specific surface area of catalysts were calculated using the multipoint Brunauer-Emmett-Teller (BET) method, as an average desorption and adsorption values in the P/P_o range of 0–0.35.The pore size distribution was calculated from the desorption curve in the whole range of pressures by using two different models, BJH (Barrett-Joyner-Halenda) and DFT (Density Functional Theory).

UV–vis diffuse reflectance spectra (DRS) were recorded by using a Shimadzu UV-2600 Spectrophotometer in a range 200–800 nm. The powder was pressed in a holder to get a flat surface before the analysis. The optical band gaps were calculated by considering indirect transitions, as typically applied to TiO_2 based samples.

Photoluminescence was recorded by using a Perkin Elmer LS-55, preparing the samples by pressing in a holder to get a flat surface before the analysis. The analyses were run by using dry powders with the following parameters: excitation wavelength: 300 nm, scanning speed of 500 nm min^{-1}, excitation slit width 2.5 nm, emission slit: 7.5 nm.

The point of zero charge was assessed by Brookhaven ZetaPALS (Zeta potential Brookhaven Instruments Corporation, USA). The Zeta potential of the samples was recorded at different pH's in water suspensions of 1 mg/L at 25 °C and the equipment run 10 cycles per measurement. The pH of samples was adjusted by using 0.3 M HCl and 1 M NaOH and the same analysis was triplicated.

The irradiation system employed for the reactivity study consisted of a flat visible LED source (electric power absorbed: 33.1 W) emitting at wavelengths greater than 425 nm (Fig. S1). A 400 mL beaker was placed containing 250 mL suspension mixed at a 1800 rpm by using a magnetic stirrer. The radiation intensity reaching the surface of the suspension was 203 W m^{-2} (measured in the 450–950 nm range by using a DeltaOhm 9721 radiometer and the matching probe). Before the runs, each sample was added progressively into 250 mL DI water (every time treating with ultrasounds for 2 min) until reaching a final transmitted radiation intensity from the bottom of the beaker of ca. 10% with respect to the transmitted light in the presence of only DI water: in this way it was assured that all particles were irradiated. The powder

weight required to have this transmittance was the one used for the reactivity tests (Table S1), carried out in water suspensions of 5 mg L^{-1} of 4-nitrophenol (4-NP), at the natural pH of 5.5. At this pH, only molecular 4-NP exists in solution and the amount of 4-nitrophenate can be neglected. This is relevant since the latter one has a strong absorption in the visible radiation and would drastically affect the reactivity under radiation greater 425 nm, such that used in the present study.

Oxygen was bubbled into the suspension for 2 h in the dark before turning the lamp on, after which the adsorbed 4-NP was checked. Then light was then switched on and oxygen was flowed during all the run. Samples were withdrawn periodically from the reactor by using a syringe and filtered using a 0.2 μm PTFE filter. The total irradiation time was 20.5 h. The extent of degradation of 4-NP was measured as a function of the visible absorbance of each sample at a wavelength of 315 nm by using a Thermo Scientific HPLC (Dionex UltiMate 3000 Photodiode Array Detector) with an Acclaim-120 C18 Reversed-phase LC column working at 25 °C (eluent: 33% water, 33% acetonitrile, 34% methanol; flow rate: 0.2 mL min^{-1}). The reproducibility of the experimental runs was always over 95%. The stability of N-TiO_2-G_1% was assessed by recycling the catalyst for 3 runs. After the each photocatalytic reaction, the suspension was centrifuged and filtered to recover the photocatalyst, which was washed with DI water, dried and used in the next cycle of 4-NP oxidation, in the same experimental conditions described above.

3. Results and discussion

GO was prepared by using a modified Hummer's method [12] and reduced using sodium borohydride. After that, Titanium tetrabutoxide (TBOT) was hydrolyzed in a controlled way, in the presence of evenly dispersed G and a nitrogen source. The obtained powder was annealed at 450 °C under nitrogen flow to limit graphene oxidative thermal degradation. The thermal treatment resulted in the degradation of excess G layers built up over the nanoparticles (Figs. 1, 2 and S2) during the annealing of the composite catalyst, thus ensuring the photocatalytic activity of the materials. EDX mapping on titanium, oxygen and carbon on a representative composite shows the very different Ti signal before and after treatment (Figs. 1 and 2), due to the degradation of G over TiO_2 particles during the annealing. Incidentally, it should be pointed out that EDX is not very sensitive for oxygen and, especially, for carbon at the low used loading.

XRD allowed to verify the successful oxidation of graphite to graphite oxide first and to graphene oxide (GO) after exfoliation, and also the reduction of graphene oxide (GO) to reduced graphene oxide (Fig. S3). In fact, the characteristic diffraction peaks of graphite, corresponding to (002) and (004) plans, disappear after oxidation, and GO peak at 10.25° disappears after reduction. The diffraction peak at 8.2°, obtained for G, can be ascribed to the establishment of a 1.1 nm interplanar spacing in the stacking of the carbon layers, similarly to what previously observed [13]. A broad (002) peak can be observed at ca. 29.0° and it can be attributed to the layer-to-layer distance (0.31 nm) [14]. The broad diffraction peak at 43° is associated to a turbostratic signal characteristic of disordered carbon nanomaterials [15]. Looking at the XRD diffractograms of N-TiO_2 and N-TiO_2-G (Fig. S4), we can observe all the characteristic peaks of brookite and rutile (25.4°, 30.8°, 48.1° for brookite; 27.4°, 41.2°, 54.3°, 56.6°, 69.0° for rutile), and exclude the presence of anatase (75.1° is an intense diffraction peak of the crystal plane (215) of anatase and, in this case, it is absent). Graphene peaks are not visible in the XRD of the composite materials, since its percentage is far below XRD detection limit. Using the Scherrer's equation [6], the rutile crystallites was 22–29 nm in size, well larger than those of brookite crystallites (11–13 nm).

The Raman spectra of graphite, graphite oxide, GO and G (Fig. S5) highlight that, upon graphite oxidization to graphite oxide, the characteristic sharp bands of the former disappear. The predominant Raman bands in GO and G are the *D* and *G* bands, and the ratio between the intensity of *D* and *G* bands looks greater for G, compared to GO, thus confirming the successful reduction of the latter one. Moreover, the 2D band is absent because both GO and G are highly defective [16].

Raman spectra of the composite materials are shown in Fig. 3, where brookite signals at ca. 150 (A_{1g}), 246 (A_{1g}), 322 (B_{1g}), 365 (B_{2g}), 402 (A_{1g}), 449 (B_{2g}), and 640 (A_{1g}) cm^{-1} can be clearly observed [17]. Rutile signals are more difficult to be identified and they correspond to frequencies of 126 (A_{1g}), 440 (E_g) and 611 (B_{1g}) cm^{-1}, as also suggested by literature [18]. However, the exact determination of rutile frequencies is hampered by the high number of brookite bands, which partially overlap with rutile bands. The Raman signals of graphene cannot be seen, due to the small amount used, and to the TiO_2 Raman background in the spectral region of the graphene Raman peaks.

After reduction of GO, the FTIR highlighted the disappearance of the band centered at 1700 cm^{-1}, assigned to C=O stretching, pointing to the effective reduction of GO to G (Fig. S6). The difference between

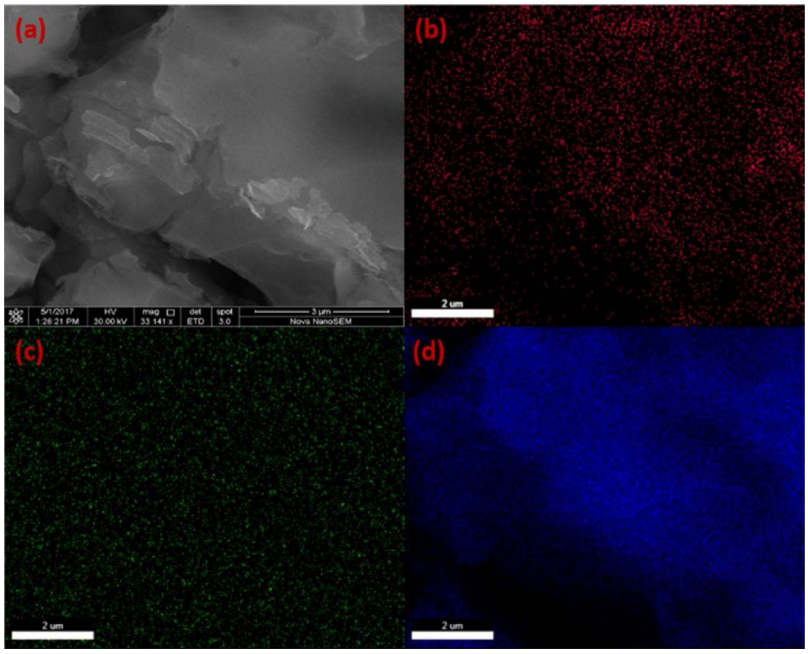

Fig. 1. EDX mapping of N-TiO_2-G_0.5% before annealing: (a) image, (b) carbon mapping, (c) titanium mapping, (d) oxygen mapping.

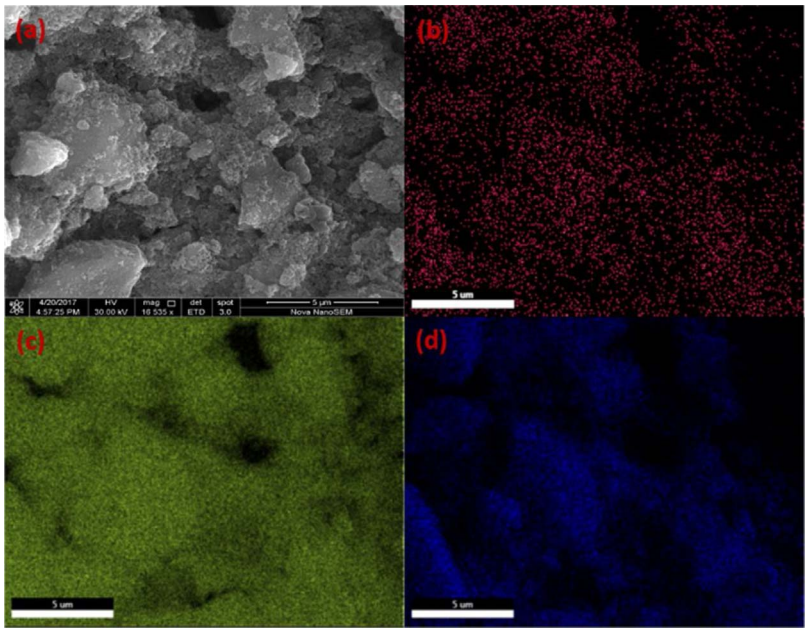

Fig. 2. EDX mapping of N-TiO_2-G_0.5% after annealing: (a) image, (b) carbon mapping, (c) titanium mapping, (d) oxygen mapping.

N-TiO_2 and N-TiO_2-G_1% is not obvious. The C═C band centered at 1600 cm^{-1} partially overlaps with −OH signals making it very difficult to appreciate any difference.

XPS surveys of GO and G also support the effective reduction of the former to the latter. As shown in high resolution carbon spectra for GO and G (Fig. 4 a and b), the oxidized carbon peaks (C−O at 286.8 eV and C═O at 288.1 eV) decreased from 36 to 21.8% and from 5.4 to 4.5%, respectively, while sp^2 carbon peak (C−C at 284.8 eV) increased from 17.9 to 28.7% after the reduction. In Fig. 4c and d, high resolution (HR) carbon spectra for N-TiO_2 with 0.1% and 1% G loadings are shown. Due to the very small G content in N-TiO_2 and the possible contamination of adventitious carbon from the atmosphere, it is difficult to conclusively attribute the sp^2 carbon signal to G. However, small increase of carbon content is observed for the higher G loading sample, possibly originated from increased G in N-TiO_2.

TEM characterization of graphite oxide, GO and G are shown in Supporting information (Fig. S7), where the 2-dimensional morphology typical of these materials with thinner and smaller particle sizes moving from graphite oxide down to G is evident. TEM of N-TiO_2 samples modified with G (Fig. 5 and Fig. S8) highlighted the presence of bigger particles of rutile (20–100 nm) with respect to brookite (5–20 nm), as suggested by XRD as well.

The significantly different size and shape of brookite and rutile was recently validated by the analysis of electron diffraction patterns (EDP) and *d*-spacing (through HRTEM) of analogous brookite-rutile samples prepared without G [6].

Fig. 5 shows that brookite and rutile nanoparticles grow on G sheets with dimensions ranging from ca. 100 to 1000 nm, and the good contact among rutile, brookite and G is remarkable. This is obviously propitious for an efficient charge transfer and stable separation of electrons and holes, as further demonstrated by photoluminescence spectra shown in the following. In samples containing 1% G, it was possible to detect G in few points, although its high transparency to the electron beam, along with the masking effects of nanoparticles on it hampered a perfect visualization (Fig. 5c and d). The EDP of an area where brookite, rutile and G were present (inset of Fig. 5a) resulted in bright circles typical of G, along with distinct spots determined by crystalline particles.

A hysteresis of type IV can be seen in the BET isotherms of all the samples (Figs. S9–14 in Supporting information), pointing to a capillary condensation in mesopores. The pore sizes are in the mesoporosity region, roughly ranging from 2.9 to 30 nm and pore size distributions are available as Supporting information. The specific surface area is smaller for the sample with 1% G, with wider pores compared to the other samples, as shown in Table 1.

In UV–vis DRS (Fig. S15) we can notice a slightly better ability to absorb visible radiation with respect to N-TiO_2, although the calculated band gap of N-TiO_2 (2.95 eV) for indirect semiconductors is very close to that of N-TiO_2-G_2% (2.93 eV), similarly to what previously reported for modified TiO_2 [20,21].

The photoluminescence (PL) emission upon excitation at 300 nm (Fig. 6) shades light on the strong improvement of charge separation on

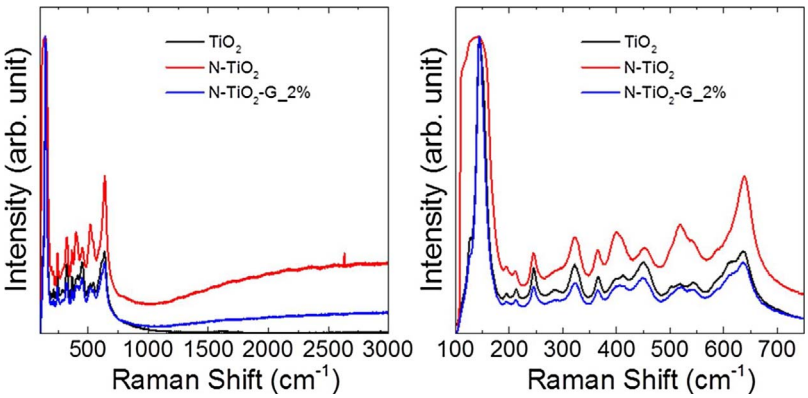

Fig. 3. Raman spectra of TiO_2, N-TiO_2, N-TiO_2-G_2%.

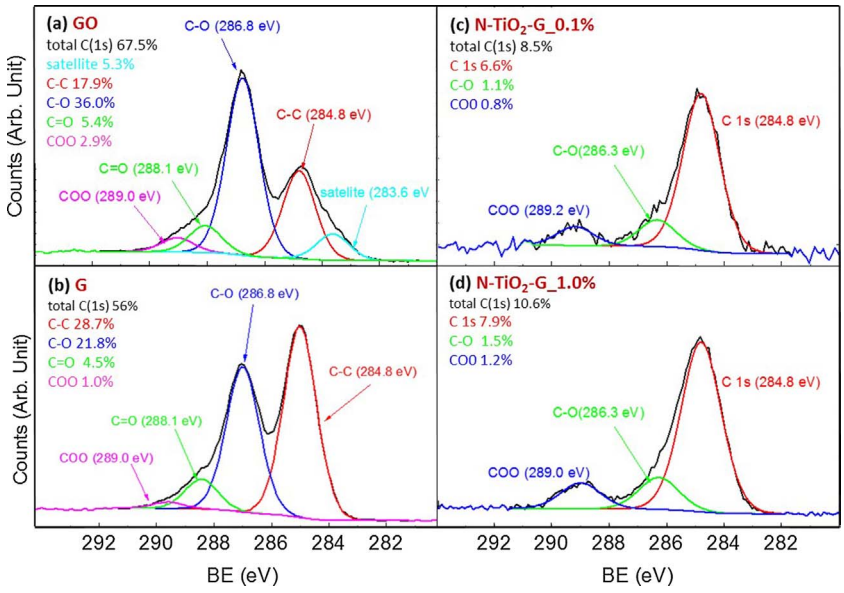

Fig. 4. XPS high resolution carbon spectra for (a) GO, (b) G, (c) N-TiO_2-G_0.1% and (d) N-TiO_2-G_1%.

the composite materials compared to TiO_2 and N-TiO_2. G surface has a positive Mulliken charge, resulting in an opposite interface dipole at the border with TiO_2 nanoparticles: consequently a strong tendency exists for electron transfer to G, resulting in an attenuation of charge recombination [22]. Accordingly, a lower photoluminescence emission can be observed in the whole emission spectrum (380–585 nm) for N-TiO_2-G_1% compared to N-TiO_2 and TiO_2. From the spectra in Fig. 6 one can notice that the shape of the emissions are similar and the main emission is centered at ca. 420 nm. The band-to-band transition occurs around this wavelength corresponding to the band gap energy. Emission at greater wavelengths is produced by electron trapping in TiO_2 oxygen vacancies and transitions from intra-band gap states to valence band. However, the intensity of the peak in the presence of G is lower compared to N-TiO_2, highlighting the ability of G to attract electrons on

Table 1
Textural properties of the catalysts under study.

	BET SSA ($m^2\ g^{-1}$)	PHW(DF model) (nm)	PR (BJH model) (nm)	TPV ($cc\ g^{-1}$)
TiO_2	41.9	4.66	8.29	0.144
N-TiO_2	56.8	3.73	7.53	0.178
N-TiO_2-G_0.1%	56.0	3.73	7.60	0.161
N-TiO_2-G_0.5%	56.8	3.90	7.62	0.159
N-TiO_2-G_1%	50.1	4.67	9.44	0.179
N-TiO_2-G_2%	59.1	3.90	8.36	0.173

SSA, specific surface area; PHW, pore half width; PR, pore radius; TPV, total pore volume.

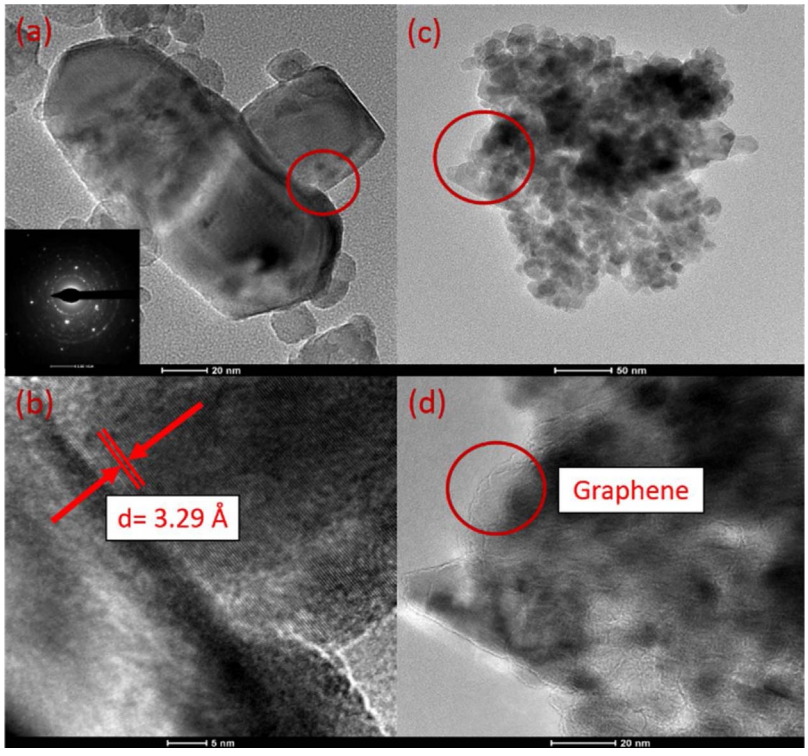

Fig. 5. TEM images of N-TiO_2-G_1%. (a) Nanoparticles of rutile and brookite (contact highlighted) with the corresponding EDP in inset; (b) crystal fringes of rutile (110) plane; (c,d) G edge highlighted in an agglomerate of particles grown on it (c,d were shown as preview in the review article [19]).

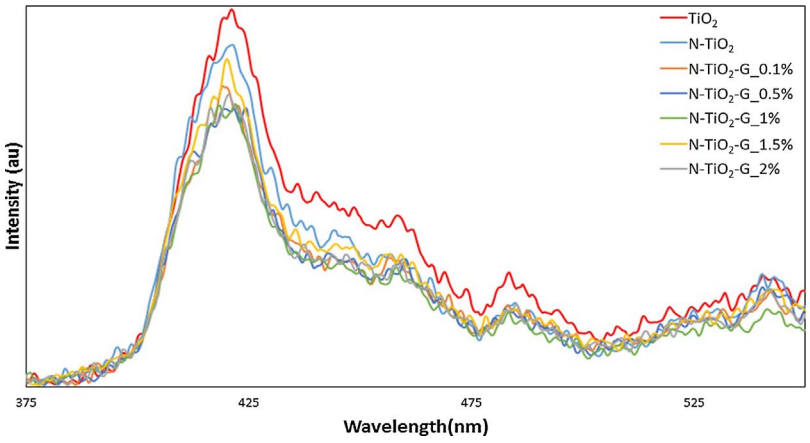

Fig. 6. Photoluminescence emission spectra of TiO_2, N-TiO_2 and N-TiO_2-G at different G loadings. Excitation wavelength: 300 nm.

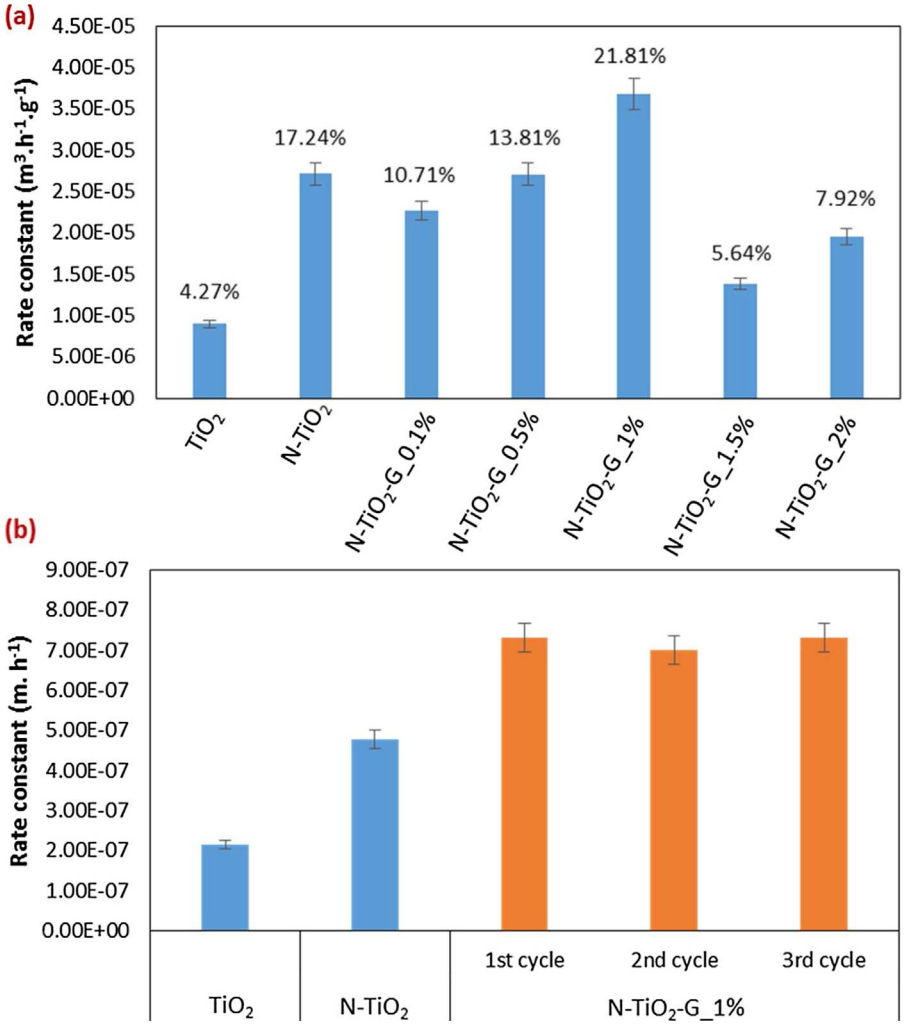

Fig. 7. Pseudo-first order constants of 4-NP conversion by using TiO_2, N-TiO_2 and N-TiO_2-G at different G loadings (a) on weight basis; (b) on surface area basis. The conversion percentage of catalyst after 5 h is reported above the error bar of each catalysts (a).

an energy level close to the conduction band of brookite and rutile and to convey them away from TiO_2, thus limiting their recombination with holes. This is possible given the work function of reduced graphene oxide (-4.5 ± 0.2 eV) [23] compared to the conduction band of TiO_2 which is -4.0 ± 0.1 eV (the N-doping does not affect this level much) [6,8].

The point of zero charge of G in water is ranging from 3 to 5 due to the presence of carboxylic acid groups and phenolic hydroxyl groups in G [24]. On the other hand, the point of zero charge of TiO_2 can be drastically different depending on the surface characteristics of the semiconductor. In the present case, the Zeta-potential analysis performed on the composite materials indicated that Nitrogen doping and G loading had a minor effect on the point of zero charges, which ranged between 4.7 and 5.3 without any trend (Supporting information, Fig. S16 and Table S2). The minor change by doping with nitrogen can be ascribed to the electronegativities of nitrogen and oxygen in TiO_2, which are not very different. On the other hand, G is not affecting the point of zero charge of photocatalysts most probably because it is located below the semiconductor nanoparticles, with a negligible interface with water molecules.

In terms of activity in the removal of 4-NP from water, all the composite catalysts showed a negligible ability to adsorb the organic species without any applied radiation. After switching the light on, the photocatalytic activity of brookite-rutile sample enhanced drastically via N-doping, whereas the contemporary N-doping and loading of 1% G, gave a further increase in the pseudo-first order kinetic constant (k) of 4-NP disappearance via photooxidation under UV-free visible radiation (Fig. 7) evaluated through an exponential best fitting procedure of the following equations:

$$-r_{4-NP} = -\frac{V}{X}\frac{dC_{4-NP}}{dt} = kC_{4-NP} \quad (1)$$

where $-r_{4\text{-NP}}$ is the disappearance rate of 4-NP, V is the reactor volume, t is the irradiation time and X is either the mass (Fig. 7a) or the surface area (Fig. 7b) of the catalyst in the reactor. The improvement of G over N-TiO_2, in terms of kinetic constant, was 40% and 60% on mass and surface basis, as showed in Fig. 7a and b, respectively. Notably, the optimum catalyst has been filtered, washed and dried after reaction and reusing it for three times did not result in any noticeable deactivation (Fig. 7b). 4-NP conversion achieved with the optimum catalyst was 45% after 22.5 h irradiation (Fig. 7a). Table 1 reveals that the best performing catalyst, N-TiO_2-G_1%, is also the one with the widest pores and the highest total pore volume. Then, porosity is relevant in affecting reactivity thanks to a favorable adsorption on catalyst surface, which is more accessible in porous particles. Specific surface area is instead the lowest for the same sample.

Although the investigation of reaction mechanism was not the aim of the present study, extensive past research has shown that, in the course of 4-NP photocatalytic oxidation, NO_2 group can be replaced by a hydroxyl group forming hydroquinone or alternatively an hydroxyl radical can enter the ortho-position activated by the phenolic group in 4-NP, producing 3,4-dihydroxynitrobenzene. Ring opening and conversion to CO_2 are further oxidation steps, although the parallel conversion to CO_2 of the starting substrate, without any formation of organic intermediates is also viable, as shown in a number of studies [25–27].

Finally, the value of the presented catalysts in the oxidation of 4-NP under low energy visible radiation was underlined by the total lack of activity, which distinguished analogous experimental runs carried out in the presence of commercial catalysts, i.e. Evonik P25 and mixtures of Sigma-Aldrich rutile and brookite (50/50 w/w).

4. Conclusion

The reported study showed that the contemporary i) N-doping and ii) growth of brookite-rutile samples on reduced graphene oxide yield a high efficiency in the oxidation of a model pollutant (4-NP) from water through photodegradation under UV-free visible radiation. The effect of reduced graphene oxide in the composite material is to: (i) improve the charge separation and (ii) extend the light absorption threshold. Likely, π-conjugation of reduced graphene oxide can play a major positive role.

Acknowledgements

Florent Ravaux and Thomas Delclos are gratefully acknowledged for their assistance at the TEM, XRD and FTIR. Abu Dhabi Education Council (ADEC Award for Research Excellence 2015 A2RE 2015, project code EX2016-000005) is gratefully acknowledged for funding. CC and YS acknowledge the Engineering and Physical Sciences Research Council (EPSRC) in the framework of the project Graphene Based Membranes (EP/K016946/1). CC, CM and YS acknowledge the UK Research Partnership Investment Funding (UKRPIF) Manchester RPIF Round 2 for use of the XPS.

Appendix A. Supplementary data

Supplementary data associated with this article can be found, in the online version, at https://doi.org/10.1016/j.jece.2017.09.042.

References

[1] G. Palmisano, M. Addamo, V. Augugliaro, T. Caronna, A. Di Paola, E. Garcia López, V. Loddo, G. Marcì, L. Palmisano, M. Schiavello, Selectivity of hydroxyl radical in the partial oxidation of aromatic compounds in heterogeneous photocatalysis, Catal. Today 122 (2007) 118–127, http://dx.doi.org/10.1016/j.cattod.2007.01.026.
[2] L. Clarizia, I. Di Somma, R. Marotta, P. Minutolo, R. Villamaina, R. Andreozzi, Photocatalytic reforming of formic acid for hydrogen production in aqueous solutions containing cupric ions and TiO_2 suspended nanoparticles under UV-simulated solar radiation, Appl. Catal. A 518 (2016) 181–188, http://dx.doi.org/10.1016/j.apcata.2015.09.020.
[3] M.J. López-Muñoz, A. Revilla, G. Alcalde, Brookite TiO_2-based materials: synthesis and photocatalytic performance in oxidation of methyl orange and As(III) in aqueous suspensions, Catal. Today 240 (2015) 138–145, http://dx.doi.org/10.1016/j.cattod.2014.05.008.
[4] O. Sacco, V. Vaiano, D. Sannino, P. Ciambelli, Visible light driven mineralization of spiramycin over photostructured N-doped TiO_2 on up conversion phosphors, J. Environ. Sci. 54 (2017) 268–276, http://dx.doi.org/10.1016/j.jes.2016.02.018.
[5] O. Diwald, T.L. Thompson, T. Zubkov, S.D. Walck, J.T. Yates, Photochemical activity of nitrogen-doped rutile TiO_2 (110) in visible light, J. Phys. Chem. B 108 (2004) 6004–6008, http://dx.doi.org/10.1021/jp031267y.
[6] O. Pikuda, C. Garlisi, G. Scandura, G. Palmisano, Micro-mesoporous N-doped brookite-rutile TiO_2 as efficient catalysts for water remediation under UV-free visible LED radiation, J. Catal. 346 (2017) 109–116, http://dx.doi.org/10.1016/j.jcat.2016.12.010.
[7] F. Peng, L. Cai, H. Yu, H. Wang, J. Yang, Synthesis and characterization of substitutional and interstitial nitrogen-doped titanium dioxides with visible light photocatalytic activity, J. Solid State Chem. 181 (2008) 130–136, http://dx.doi.org/10.1016/j.jssc.2007.11.012.
[8] (a) A.K. Geim, Graphene: status and prospects, Science 5934 (2009) 1530–1534; (b) G. Žerjav, M.S. Arshad, P. Djinović, I. Junker, J. Kovac, J. Zavašnik, A. Pintar, Improved electron-hole separation and migration in anatase TiO_2 nanorod/reduced graphene oxide composites and their significance on photocatalytic performance, Nanoscale 9 (2017) 4578–4592, http://dx.doi.org/10.1039/C7NR00704C.
[9] A.P. Bhirud, S.D. Sathaye, R.P. Waichal, J.D. Ambekar, C.-J. Park, B.B. Kale, In-situ preparation of N-TiO_2/graphene nanocomposite and its enhanced photocatalytic hydrogen production by H_2S splitting under solar light, Nanoscale 7 (2015) 5023–5034, http://dx.doi.org/10.1039/c4nr06435f.
[10] L. Luo, Y. Yang, A. Zhang, M. Wang, Y. Liu, L. Bian, F. Jiang, X. Pan, Hydrothermal synthesis of fluorinated anatase TiO_2/reduced graphene oxide nanocomposites and their photocatalytic degradation of bisphenol A, Appl. Surf. Sci. 353 (2015) 469–479, http://dx.doi.org/10.1016/j.apsusc.2015.06.150.
[11] M.S.A. Sher Shah, A.R. Park, K. Zhang, J.H. Park, P.J. Yoo, Green synthesis of biphasic TiO_2 – reduced graphene oxide nanocomposites with highly enhanced photocatalytic activity, ACS Appl. Mater. Interfaces 4 (2012) 3893–3901, http://dx.doi.org/10.1021/am301287m.
[12] J. Song, X. Wang, C.-T. Chang, Preparation and characterization of graphene oxide, J. Nanomater. 2014 (2014) 1–6, http://dx.doi.org/10.1155/2014/276143.
[13] M. Kumar, S. Kumar, Stacking of ultra-thin reduced graphene oxide nanoparticles in supramolecular structures for optoelectronic applications, RSC Adv. 5 (2015) 14871–14878, http://dx.doi.org/10.1039/C4RA15705B.
[14] D. Geng, S. Yang, Y. Zhang, J. Yang, J. Liu, R. Li, T.-K. Sham, X. Sun, S. Ye, S. Knights, Nitrogen doping effects on the structure of graphene, Appl. Surf. Sci. 257 (2011) 9193–9198, http://dx.doi.org/10.1016/j.apsusc.2011.05.131.
[15] I. Roy, G. Sarkar, S. Mondal, D. Rana, A. Bhattacharyya, N.R. Saha, A. Adhikari, D. Khastgir, S. Chattopadhyay, D. Chattopadhyay, Synthesis and characterization of graphene from waste dry cell battery for electronic applications, RSC Adv. 6 (2016) 10557–10564, http://dx.doi.org/10.1039/c5ra21112c.
[16] A. Eckmann, A. Felten, I. Verzhbitskiy, R. Davey, C. Casiraghi, Raman study on defective graphene: effect of the excitation energy, type, and amount of defects, Phys. Rev. B 88 (2013) 35426, http://dx.doi.org/10.1103/PhysRevB.88.035426.
[17] M.N. Iliev, V.G. Hadjiev, A.P. Litvinchuk, Raman and infrared spectra of brookite (TiO_2), Exp. Theory (2013), http://dx.doi.org/10.1016/j.vibspec.2012.08.003.
[18] H. Jensen, K.D. Joensen, J.-E. Jørgensen, J.S. Pedersen, G. Søgaard, Characterization of nanosized partly crystalline photocatalysts, J. Nanopart. Res. 6 (2004) 519–526, http://dx.doi.org/10.1007/s11051-004-1714-3.
[19] L.Y. Ozer, C. Garlisi, H. Oladipo, M. Pagliaro, S.A. Sharief, A. Yusuf, S. Almheiri, G. Palmisano, Inorganic semiconductors-graphene composites in photo(electro) catalysis: synthetic strategies, interaction mechanisms and applications, J. Photochem. Photobiol. C: Photochem. Rev. (2017), http://dx.doi.org/10.1016/j.jphotochemrev.2017.06.003.
[20] L.-W. Zhang, H.-B. Fu, Y.-F. Zhu, Efficient TiO_2 photocatalysts from surface hybridization of TiO_2 particles with graphite-like carbon, Adv. Funct. Mater. 18 (2008) 2180–2189, http://dx.doi.org/10.1002/adfm.200701478.
[21] M. Minella, F. Sordello, C. Minero, Photocatalytic process in TiO_2/graphene hybrid materials. Evidence of charge separation by electron transfer from reduced graphene oxide to TiO_2, Catal. Today 281 (2017) 29–37, http://dx.doi.org/10.1016/j.cattod.2016.03.040.

[22] M. Aliofkhazraei, N. Ali, W.I. Milne, C.S. Ozkan, S. Mitura, J.L. Gervasoni, Graphene Science Handbook Fabrication Methods, CRC Press, 2016.
[23] L. Sygellou, G. Paterakis, C. Galiotis, D. Tasis, Work function tuning of reduced graphene oxide thin films, J. Phys. Chem. C 120 (2016) 281–290, http://dx.doi.org/10.1021/acs.jpcc.5b09234.
[24] S. Navalon, A. Dhakshinamoorthy, M. Alvaro, H. Garcia, Carbocatalysis by graphene-based materials, Chem. Rev. 114 (2014) 6179–6212, http://dx.doi.org/10.1021/cr4007347.
[25] M.S. Dieckmann, K.A. Gray, A comparison of the degradation of 4-nitrophenol via direct and sensitized photocatalysis in TiO_2 slurries, Water Res. 30 (1996) 1169–1183, http://dx.doi.org/10.1016/0043-1354(95)00240-5.
[26] N. San, A. Hatipoğlu, G. Koçtürk, Z. Çınar, Photocatalytic degradation of 4-nitrophenol in aqueous TiO_2 suspensions: theoretical prediction of the intermediates, J. Photochem. Photobiol. A 146 (2002) 189–197, http://dx.doi.org/10.1016/S1010-6030(01)00620-7.
[27] A. Di Paola, V. Augugliaro, L. Palmisano, L. Pantaleo, E. Savinov, Heterogeneous photocatalytic degradation of nitrophenols, J. Photochem. Photobiol. A 155 (2003) 207–214, http://dx.doi.org/10.1016/S1010-6030(02)00390-8.